

An investigation of the origin of soft X-ray excess emission from Narrow-line Seyfert 1 galaxies Akn 564 and Mrk 1044

G. C. Dewangan¹, R. E. Griffiths¹, Surajit Dasgupta² & A. R. Rao²

ABSTRACT

We investigate the origin of the soft X-ray excess emission from narrow-line Seyfert 1 galaxies Akn 564 and Mrk 1044 using *XMM-Newton* observations. We find clear evidence for time delays between the soft and hard X-ray emission from Akn 564 based on a ~ 100 ks long observation. The variations in the 4 – 10 keV band lag behind that in the 0.2 – 0.5 keV band by 1768 ± 122 s. The full band power density spectrum (PDS) of Akn 564 has a break at $\sim 1.2 \times 10^{-3}$ Hz with power-law indices of ~ 1 and ~ 3 below and above the break. The hard (3 – 10 keV) band PDS is stronger and flatter than that in the soft (0.2 – 0.5 keV) band. Based on a short observation of Mrk 1044, we find no correlation between the 0.2 – 0.3 keV and 5 – 10 keV bands at zero lag. These observations imply that the soft excess is not the reprocessed hard X-ray emission. The high resolution spectrum of Akn 564 obtained with the reflection grating spectrometer (RGS) shows evidence for a highly ionized and another weakly ionized warm absorber medium. The smeared wind and blurred ionized reflection models do not describe the EPIC-pn data adequately. The spectrum is consistent with a complex model consisting of optically thick Comptonization in a cool plasma for the soft excess and a steep power-law, modified by two warm absorber media as inferred from the RGS data and the foreground Galactic absorption. The smeared wind and optically thick Comptonization models both describe the spectrum of Mrk 1044 satisfactorily, but the ionized reflection model requires extreme parameters. The data suggest two component corona – a cool, optically thick corona for the soft excess and a hot corona for the power-law component. The existence of a break in the soft band PDS suggests a compact cool corona that can either be an ionized surface of the inner disk or an inner optically thick region coupled to a truncated disk. The steep power-law component is likely arising from an extended region.

Subject headings: accretion, accretion disks – galaxies: active – X-rays: galaxies

1. Introduction

A significant fraction of type 1 active galactic nuclei (AGN) show ‘soft X-ray excess emission’ above a power-law continuum, usually identified as the steepening of the X-ray continuum below ~ 2 keV. This soft excess emission was first observed by *HEAO-1* (Pravdo et al. 1981), and *EXOSAT* (Arnaud et al. 1985; Singh et al. 1985). Boller, Brandt, & Fink (1996) showed that AGN

with the steepest soft X-ray spectra tend to lie at the lower end of the $H\beta$ line width distribution. These AGN with $\text{FWHM}_{H\beta} \lesssim 2000 \text{ km s}^{-1}$ are classified as the narrow-line Seyfert 1 galaxies (NLS1; Osterbrock & Pogge 1985), and are distinguished from the bulk of the Seyfert 1 galaxies. In addition to the strong soft X-ray excess below 2 keV and narrower permitted lines, NLS1 also show a number of extreme properties e.g., steep 2 – 10 keV power-law continuum, extreme X-ray variability and strong Fe II emission. These properties are all related and one suggestion is that NLS1 are the supermassive black hole analogue of stellar mass black hole X-ray binaries (BHB) in their ‘high/soft’ state.

¹Department of Physics, Carnegie Mellon University, 5000 Forbes Avenue, Pittsburgh, PA 15213 USA; email: gulabd@cmu.edu; griffith@seren.phys.cmu.edu

²Department of Astronomy & Astrophysics, Tata Institute of Fundamental Research, Mumbai, 400005 India; email: surajit@tifr.res.in; arrao@tifr.res.in

However, the origin of the soft X-ray excess emission has remained a major problem in AGN research over the past two decades. The soft excess emission is a smooth continuum component rather than a blend of emission/absorption features as revealed by *Chandra* and *XMM-Newton* grating observations (e.g., Turner et al. 2001a; Collinge et al 2001). When described as a thermal component, the soft excess emission has a remarkably constant temperature ($\sim 100\text{--}200$ eV) across AGN with a wide range of black hole masses (Czerny et al. 2003; Gierlinski & Done 2004; Crummy et al. 2006). There are a number of ideas that have been proposed to explain the origin of the soft excess component. Pounds, Done & Osborne (1995) pointed out the similarity of the X-ray spectrum of NLS1 and Cyg X-1 in its high state (HS) and suggested that the soft excess could be the optically thick emission from an accretion disk. However, the observed soft excess emission is too hot for a disk around a supermassive black hole. One possibility is that there is a cool, optically thick Comptonizing region in addition to a hot (~ 100 keV), optically thin ($\tau \sim 1$) region producing the high energy power-law emission. The cool region can Comptonize the disk photons and smoothly connect the disk emission up to soft X-ray energies (Magdziarz et al. 1998). Gierlinski & Done (2004) tested this model using high quality *XMM-Newton* spectra of 26 radio-quiet PG quasars. Although the spectra are well described by the Comptonization model, the temperature of the cool Comptonizing region is remarkably constant despite a large range in the black hole masses. They proposed that the observed soft excess is an artifact of heavily smeared, strong partially ionized absorption (see also Gierlinski & Done 2006; Schurch & Done 2006). Another possibility is that the emission is dominated by ionized Compton reflection. This can happen if the disk is clumpy at high accretion rates, thus hiding the hard X-ray source among many clumps. The ionized reflection can explain the observed soft excess emission (Fabian et al. 2002). The last two models, based on relativistically smeared absorption and ionized reflection, relate the soft excess emission to atomic processes and therefore provide a natural explanation for its constant temperature for AGN with a wide range in their black hole masses.

The three models, cool Comptonization, ion-

ized reflection and heavily smeared absorption, all result in statistically equally good fits. The fitting criteria are not sufficient to discriminate among them (Sobolewska & Done 2005). Variability properties of the soft and hard X-ray emission and the relationship between them may provide strong constraints on the above models for the soft excess emission. A 35 day long *ASCA* monitoring observation of the NLS1 galaxy Akn 564 revealed a distinction in the variability of the soft excess and power-law components on a time scale of weeks, with the soft excess emission varying by a factor of ~ 6 compared to a factor of ~ 4 in the power-law component (Turner et al. 2001b). Similarly, a long ~ 10 days *ASCA* observation of the NLS1 galaxy IRAS 13224-3809 suggested that the soft excess component dominates the observed variability on a time scale of $\sim a\text{ week}$, but on shorter time scales (~ 20000 s), the power-law component appears to dominate the variability (Dewangan et al. 2002). A 12 day long *ASCA* observation of another NLS1 galaxy Ton S180 suggested that the soft excess and the power-law fluxes are not well correlated on time scales of ~ 1000 s (Romano et al. 2002). These long *ASCA* observations suggest two separate continuum component unlike the heavily smeared, ionized absorption model based on a single continuum component. Gallo et al. (2004) found evidence for alternate leads and lags between the 0.3 – 0.8 keV and 3 – 10 keV band emission from the NLS1 galaxy IRAS 13224-3809. Dasgupta & Rao (2006) reported energy dependent delay between the soft and hard X-ray emission in Mrk 110. These observations suggest different emitting regions for the soft excess and the power-law component from NLS1 galaxies. In this paper, we use *XMM-Newton* observations of two NLS1 galaxies Akn 564 and Mrk 1044 to study the variability properties of the soft and hard X-ray emission and investigate the origin of the soft excess emission. In Section 2, we outline the *XMM-Newton* observations of Akn 564 and Mrk 1044. We describe the temporal analysis in Section 3 and spectral analysis in Section 4 and discuss the results in Section 5.

2. Observation and Data Reduction

Akn 564 was observed by *XMM-Newton* on 2005 January 04 (ObsID: 0206400101) for an exposure time of 100 ks. Mrk 1044 was ob-

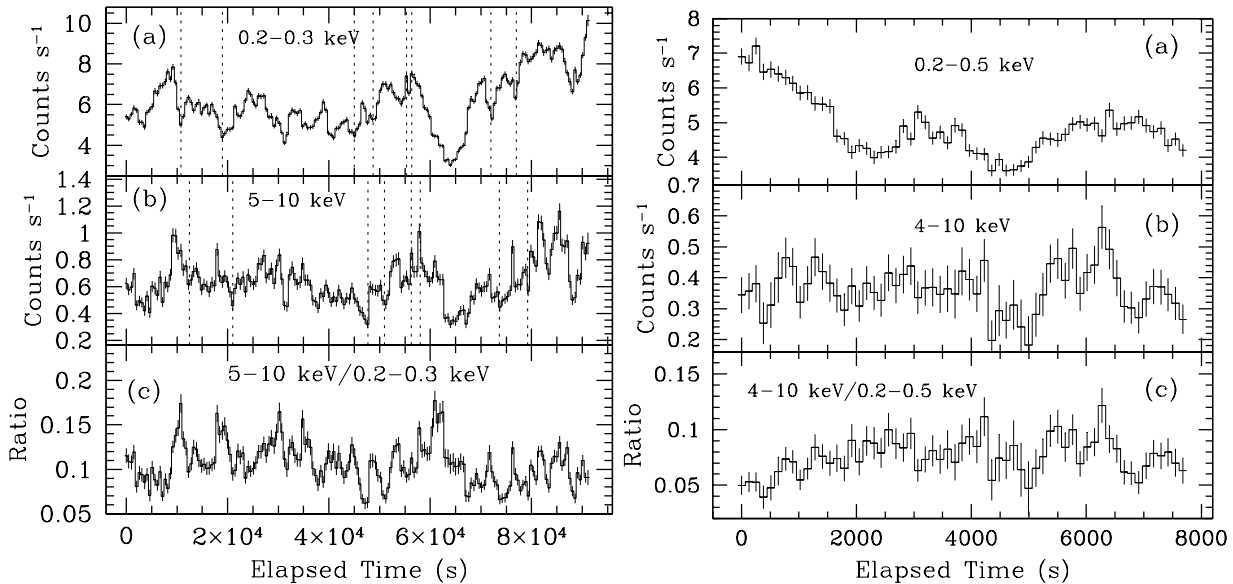


Fig. 1.— *XMM-Newton* light curves and hardness ratio of Akn 564 and Mrk 1044. *Left*: Combined EPIC-pn and MOS light curves of Akn 564 in the bands 0.2 – 0.3 keV and 5 – 10 keV bands and the hardness ratio. The bin sizes are 512 s. Vertical dotted lines mark the dips and peaks in the 0.2 – 0.3 keV and 5 – 10 keV light curves that show possible evidence for a delay. *Right*: Combined EPIC-pn and MOS light curves of Mrk 1044 in the 0.2 – 0.5 keV and 2 – 10 keV bands and the hardness ratio. The bin sizes are 128 s. The soft and hard band light curves do not appear to be strongly correlated.

served by *XMM-Newton* on 2002 July 23 (ObsID: 0112600301) for 8 ks. The EPIC-pn and MOS cameras (Strüder et al. 2001; Turner et al. 2001a) were operated in the small window mode using the medium filter during both the observations. The data were reduced using version 6.5.0 of the SAS software. Examination of the background rate above 10 keV showed that the observation of Akn 564 was partly affected by the flaring particle background before an elapsed time of 7.5 ks and this early period was therefore excluded to obtain a continuous exposure with steady background. For temporal analysis, we used all the pn and MOS events with patterns ≤ 12 and a continuous exposure of 91.3 ks during which both the pn and MOS cameras operated simultaneously. There were three short duration (< 1000 s), small amplitude background flares (maximum count rate ~ 2 counts s^{-1} above 10 keV) during the observation of Mrk 1044. The varying background contribution to the source was corrected by subtracting the background rate. For spectral analysis, we chose a count rate cut-off criterion to exclude the high particle background. In case of Akn 564, the

MOS data are affected with photon pile-up. In order to achieve the best possible spectral resolution and to have the best spectral calibration, we chose the EPIC-pn data and used the good X-ray events (FLAG=0) with pattern zero (single pixel events) for Akn 564. For Mrk 1044, we used the good EPIC-pn events with pattern 0 – 4 (single and double pixel events). We used circular regions with radii of $40''$, centered at the peak position of Akn 564 and Mrk 1044, to extract the source spectra. We also extracted background spectra from appropriate nearby circular regions, free of sources.

We also processed the RGS data obtained from the long observation of Akn 564. We extracted the first order source and the background spectra by making the spatial, order selections on the processed event files, and calibrated by applying the most recent calibration data. We also used a temporal filter to exclude the high particle background based on a count rate cut-off criterion. We have used the ISIS (version 1.4.7) spectral fitting environment (Houck & Denicola 2000; Houck 2002) for

power and energy spectral analysis. Unless otherwise stated, all errors are quoted at 90% confidence level.

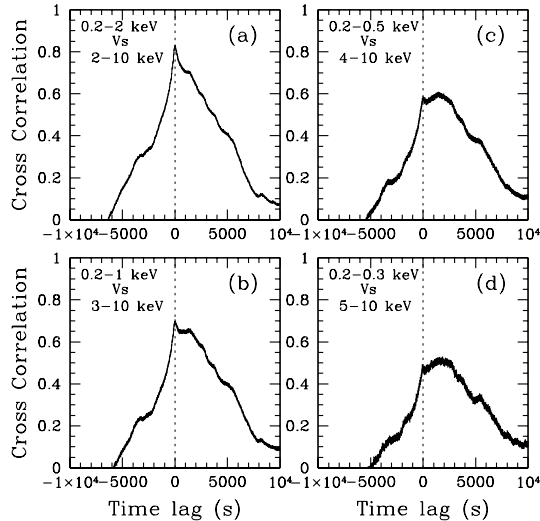


Fig. 2.— Cross correlation function between soft and hard X-ray light curves of Akn 564: (a) 0.2 – 2 keV – 2 – 10 keV, (b) 0.2 – 1 keV Vs 3 – 10 keV, (c) 0.2 – 0.5 Vs 4 – 10 keV and (d) 0.2 – 0.3 keV Vs 5 – 10 keV. The time delays refer to the soft band. Positive peaks imply that the variations in the hard band lag that in the soft band.

3. Temporal analysis

3.1. Akn 564

For temporal analysis, we combined the pn and MOS data to increase the signal-to-noise ratio. In order to study cross-correlation between different energy bands, we extracted light curves in several energy bands 0.2 – 0.3, 0.2 – 0.5, 0.2 – 1, 0.2 – 2, 2 – 10, 3 – 10, 4 – 10 and 5 – 10 keV with time bins of 64 s. Figure 1 shows the light curves of Akn 564 in the 0.2 – 0.3 and 5 – 10 keV bands rebinned to 512 s. X-ray emission from Akn 564 is highly variable. The 0.2 – 0.3 keV band light curve shows a trough-to-peak variations by a factor of ~ 3.3 , while the hard band (5 – 10 keV) shows a trough-to-peak variation by a factor of ~ 3.6 . Although the 0.2 – 0.3 keV and 5 – 10 keV band light curves appear to be correlated, the most rapid variability is seen in the hard band. A visual comparison of the light curves suggests that variations in the hard band appear to lag those in the soft band.

To investigate further, we have performed cross-correlation and power spectral analysis.

3.1.1. Cross Correlation Analysis

We have computed cross-correlation function (CCF) using the XRONOS program `crosscor`. We used the slow direct Fourier algorithm to compute the CCF between the soft and hard band light curves with 64 s bins. Figure 2 shows the CCFs as a function of time delay between the energy bands (a) 0.2 – 2 keV and 2 – 10 keV, (b) 0.2 – 1 keV and 3 – 10 keV, (c) 0.2 – 0.5 keV and 4 – 10 keV and (d) 0.2 – 0.3 keV and 5 – 10 keV. The 0.2 – 2 keV and 2 – 10 keV band light curves are strongly correlated without any time delay as indicated by the sharp peak at zero lag. However, the strength of the sharp peak decreases with the increase in the separation between the soft and hard bands. In the CCF of 0.2 – 1 keV and 3 – 10 keV band light curves, the sharp peak weakens and another broad peak at positive time lags becomes relatively stronger. The broad peak dominates the CCF for the 0.2 – 0.5 keV and 4 – 10 keV band light curves and only a weaker sharp peak is seen. The sharp peak is not clearly seen in the CCF between 0.2 – 0.3 keV and 5 – 10 keV bands, only the broad peak is seen. Thus the hard 4 – 10 keV or 5 – 10 keV band clearly lags the soft 0.2 – 0.5 keV or 0.2 – 0.3 band.

It is hard to assess the statistical significance of the time lag based on model fitting to the CCF using the traditional χ^2 minimization technique. The reasons are (i) the shape of the CCF is generally complex, (ii) the CCF data points are not independent and (iii) the errors are not normally distributed. Therefore, we have adopted a model independent way, following Peterson et al. (1998), to measure the time lag. The principal source of uncertainty in the time lag between two long, continuous light curves is the uncertainty in the observed count rates. To account for this uncertainty, we have performed Monte Carlo simulations using IDL (version 6.3). We simulated 1000 pairs of soft and hard band lightcurves by modifying the observed count rates by random Gaussian deviates assuming that the errors on the observed count rates are normally distributed. We calculated the time lag between each pair of the simulated soft and hard band light curves as the centroid of the CCF based on all points with cor-

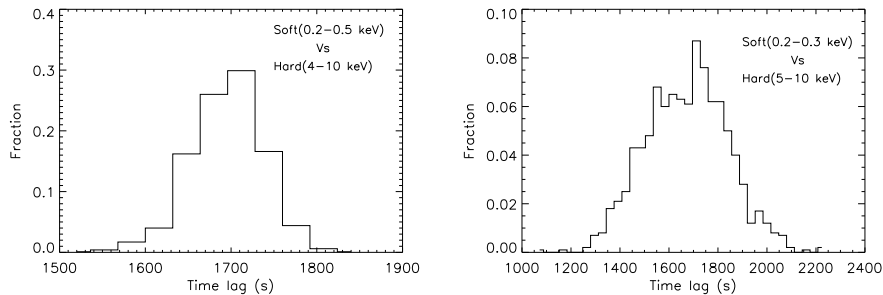


Fig. 3.— Distributions of time lags obtained from the simulated soft and hard band lightcurves. *Left:* Time-lag distribution between 0.2 – 0.5 and 4 – 10 keV bands. *Right:* Time-lag distribution between 0.2 – 0.3 and 5 – 10 keV bands.

relation coefficients in excess of 0.4. Figure 3 shows the distribution of time lags between the 0.2 – 0.5 keV and 4 – 10 keV bands. We calculated the time lag between the observed soft and hard bands as the centroid of the CCF and the errors on the time lag by directly integrating the time-lag distribution over a range to obtain 68%, 90% or 99% confidence level. Thus we measured the time lag between the 0.2 – 0.5 and 4 – 10 keV bands to be 1768 ± 92 s (68%), ± 122 s (90%) or ± 191 s (99%). A similar procedure resulted in the time lag between the 0.2 – 0.3 and 5 – 10 keV to be 1767 ± 196 s (68%), ± 320 s (90%) or ± 462 s (99%).

We have also searched for variations in the CCF or time delay. For this purpose, we divided both 0.2 – 0.5 keV and 4 – 10 keV light curves into nine equal segments with lengths 10.1 ks and computed the CCFs for each segment. The nine CCFs are plotted in Figure 4. The CCFs are not similar. There is no or weak correlation between the soft and hard band light curves in the segments II-VI and VIII. In segment IV, the soft and hard band appear to be weakly anti-correlated with a soft band lead of ~ 1200 s. The two bands are strongly correlated without any lag for the segments I & IX, while for the segments VII and VIII, the hard band lags behind the soft band. For these segments, the time lag varies from $\sim 900 - 2900$ s. In segment VII, the soft and hard band appear to anti-correlate at a lag of ~ -3000 s. Brinkmann, Papadakis & Raeth (2007) have employed the sliding window technique to study the cross-correlation properties of Akn 564 between the 0.3 – 1 keV

and 3 – 10 keV bands using the same data. There results are similar to the presented here if we note that the first 7.5 ks of data were excluded from our analysis. The leads and lags in the X-ray emission from Akn 564 are also similar to the alternate leads and lags in 4500 s intervals found between the 0.3 – 0.8 keV and 3 – 10 keV band X-ray emission from IRAS 13224-3809 by Gallo et al. (2004).

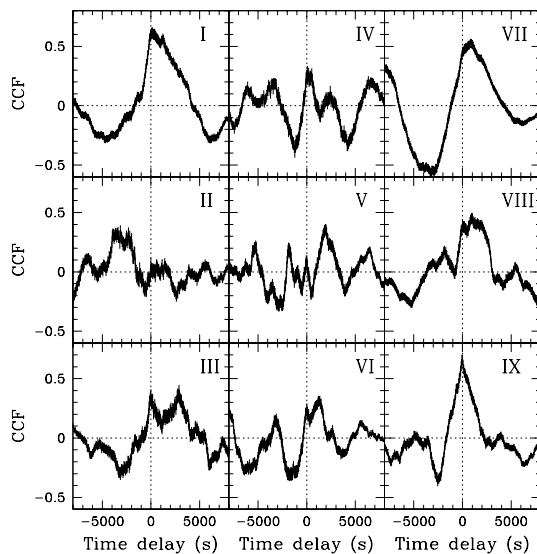


Fig. 4.— Cross correlation functions of 0.2 – 0.5 keV and 4 – 10 keV band lightcurves for Akn 564. The CCFs have been derived by splitting both 0.2 – 0.5 keV and 4 – 10 keV lightcurves into nine segments. Each segment has a length of 10.1 ks.

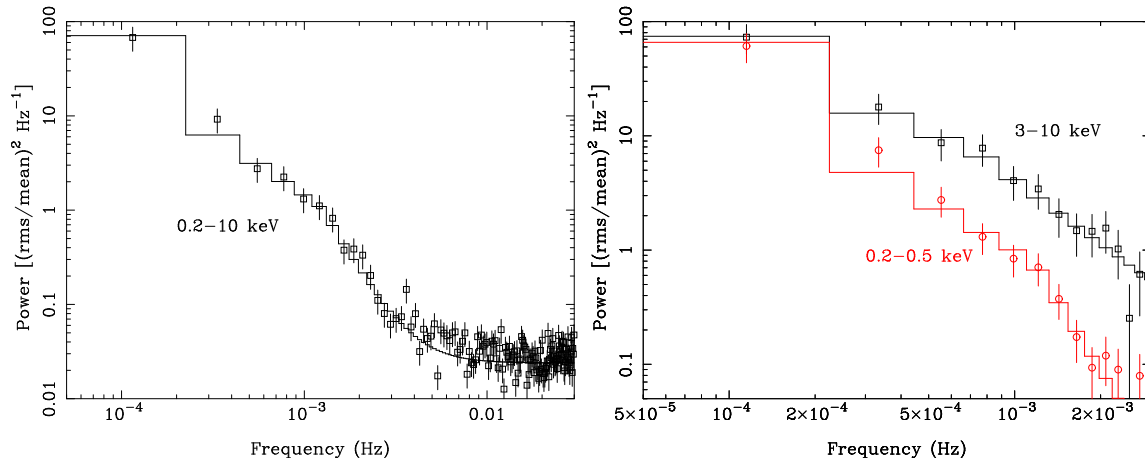


Fig. 5.— *Left*: Power density spectra of Akn 564 in the full band 0.2 – 10 keV. The contribution due to the Poisson noise has not been subtracted. *Right*: Power density spectra in the soft (0.2 – 0.5 keV) and hard (3 – 10 keV) bands, derived from the combined EPIC-pn and MOS data. The constant power expected from the Poisson errors have been subtracted. The best-fitting broken power-law models are also shown. The soft band power density spectrum is clearly steeper and weaker than the hard band power density spectrum.

3.1.2. The power density spectra

To make a further study of the variability properties of Akn 564, we have calculated power density spectra (PDS) of Akn 564 from the combined pn+MOS lightcurves in the full (0.2–10 keV), soft (0.2–0.5 keV) and hard (3–10 keV) bands, sampled at 16 s. We used the slow algorithm implemented in the XRONOS program ‘powspec’. Following Papadakis & Lawrence (1993), we rebinned the PDS in logarithmic space with a binsize of 20 and performed the fitting within the ISIS (version 1.4.5) spectral fitting environment. We converted the PDS to equivalent energy spectra (power \rightarrow counts/bin; Hz \rightarrow keV) using the `sitar` timing package. We fitted the PDS with a simple power-law model. We also used a constant to account for the power arising from the Poisson noise. The simple power-law model resulted in an unacceptable fit (minimum $\chi^2 = 225.2$ for 139 degrees of freedom (dof)). We then replaced the power-law with a broken power-law model. This model resulted in the minimum $\chi^2 = 169.2$ for 137 dof. The broken power-law model provided an improved fit at a statistical significance level of $> 99.99\%$ compared to the power-law model according to the maximum likelihood ratio test. Thus we conclude that the PDS of Akn 564 has a break at $(1.2 \pm 0.3) \times 10^{-3}$ Hz with power-law indices $1.3^{+0.1}_{-0.2}$ below the break

and $3.2^{+0.5}_{-0.4}$ above the break. The break frequency reported here is similar to the high frequency break at $\sim 2 \times 10^{-3}$ Hz discovered by Papadakis et al. (2002) based on ASCA data (see also Alvaro et al. 2006). The constant power due to Poisson noise is 0.024 ± 0.0012 (rms/mean) 2 Hz $^{-1}$. The PDS and the best-fit broken power-law plus constant model are plotted in Figure 5. The power arising from the Poisson errors have not been subtracted.

We also fitted the power-law and broken power-law models to the soft (0.2–0.5 keV) and hard (3–10 keV) PDS of Akn 564. The power-law model resulted in an unacceptable fit to the PDS in the soft band ($\chi^2 = 193.2$ for 139 dof) with power-law index of 1.7 ± 0.1 . The broken power-law model provided a better fit ($\chi^2/dof = 160.9/137$) with power-law indices $1.4^{+0.1}_{-0.2}$ and $4.0^{+1.8}_{-1.3}$ before and after the break frequency $1.1^{+0.2}_{-0.6} \times 10^{-3}$ Hz. This is an improvement over the power-law fit at a significance level of $> 99.99\%$ based on the maximum likelihood ratio test. The power-law model provided an acceptable fit to the hard band PDS ($\chi^2 = 138.4$ for 139 dof) with an index of 1.2 ± 0.1 . The broken power-law model resulted in an improved fit ($\chi^2/dof = 127.2/137$) with indices < 1.0 (90% upper limit) and $1.8^{+0.5}_{-0.4}$ before and after the break frequency $< 1.2 \times 10^{-3}$ Hz (90% upper limit). This is an improvement over the

power-law model at a level of 99.6% significance level. However, the parameters are not well determined. We have plotted the soft and hard band PDS and the best-fit broken power-law models in Fig. 5 (*right panel*). Clearly the soft band PDS is steeper than the hard band PDS. This implies that the X-ray emission in the hard band varies more than that in the soft band on shorter time scales.

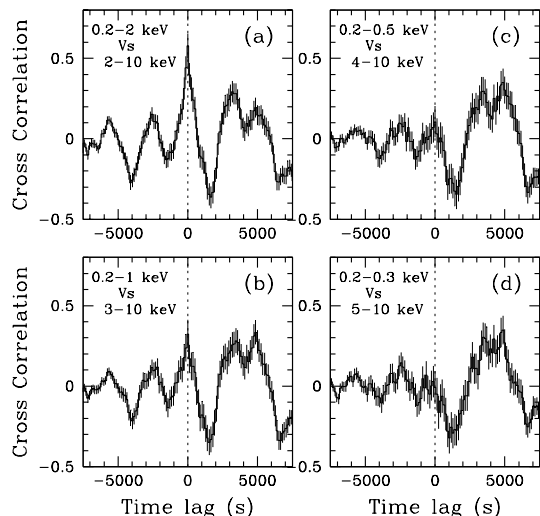


Fig. 6.— Cross correlation function between soft and hard X-ray light curves of Mrk 1044: (a) 0.2 – 2 keV – 2 – 10 keV, (b) 0.2 – 1 keV Vs 3 – 10 keV, (c) 0.2 – 0.5 Vs 4 – 10 keV and (d) 0.2 – 0.3 keV Vs 5 – 10 keV. The time delays refer to the soft band. Positive peaks imply that the variations in the hard band lag that in the soft band.

3.2. Mrk 1044

As stated above, the observation of Mrk 1044 was affected by short-duration, weak flares. Therefore, the source light curves were corrected for background contribution using appropriate background light curves extracted from blank sky regions. The combined pn+MOS and background corrected light curves of Mrk 1044 are shown in Fig. 1 (right). X-ray emission from Mrk 1044 is variable with trough-to-peak variations of ~ 2 (0.2 – 0.5 keV) and ~ 3 (4 – 10 keV). However, the 0.2 – 0.5 keV and 4 – 10 keV light curves do not appear to be strongly correlated.

The cross correlations between the soft and hard bands are plotted in Figure 6. Similar to

Akn 564, the 0.2 – 2 keV and 2 – 10 keV bands are strongly correlated without any delay and the strength of this correlation decreases with the interval between the soft and hard bands. There is no correlation between the 0.2 – 0.3 keV and 5 – 10 keV bands at zero lag. There is a weak anti-correlation at a positive delay of ~ 1000 s and a weak correlation at positive delays of 3000 – 5000 s. As the CCF for Mrk 1044 is based on a short 7.9 ks observation, the CCF is likely only one representation of many possible cross correlations similar to that seen for Akn 564.

4. Spectral Analysis

We have performed spectral modeling of Akn 564 and Mrk 1044. We present the results based on the high signal-to-noise pn data for both Akn 564 and Mrk 1044 and the high resolution RGS data for Akn 564. We note that Papadakis et al. (2007) have performed a detailed spectral analysis of Akn 564 using the same observation. The purpose here is to investigate the alternative models for the origin of the soft X-ray excess emission. All the spectra were analyzed with the Interactive Spectral Interpretation System (ISIS, version 1.4.5). The pn data were grouped to a minimum of 100 and 20 counts per spectral channel for Akn 564 and Mrk 1044, respectively. We consider a model fit as statistically unacceptable if the the null hypothesis can be rejected at more than 95% significance. The errors on the best-fit spectral parameters are quoted at a 90% confidence level. Below we use narrow Gaussian line components with their widths fixed at $\sigma = 10$ eV that are unresolved by the EPIC-pn data.

4.1. The soft X-ray excess emission

NLS1 galaxies are known to show strong soft X-ray excess emission below ~ 2 keV. To show this soft excess, first we fitted a simple absorbed power law (PL) model to the EPIC-pn spectra above 3 keV (3 – 10 keV for Mrk 1044 and 3 – 11 keV for Akn 564). The simple PL model resulted in minimum $\chi^2 = 527.4$ for 519 dof and 119.0 for 127 dof for Akn 564 and Mrk 1044, respectively, thus providing good fits to the 3 – 10 keV pn data. We have plotted the ratio of the pn data and the best-fit PL model in Figure 7 after extrapolating the model to low energies. The plots clearly show

strong soft excess emission below ~ 2.5 keV and possible iron $K\alpha$ lines near ~ 6.4 keV in the spectra of both the NLS1. The soft X-ray excess emission from NLS1 are usually well described by a simple blackbody or a multicolor disk blackbody (MCD). Addition of the MCD component to the absorbed PL improved the fit. The fit was reasonably good for Mrk 1044 ($\chi^2/dof = 628.0/541$). Addition of a narrow Gaussian line at ~ 6.4 keV further improved the fit ($\chi^2/dof = 611.7/539$). The best-fit parameters of the MCD+PL model for Mrk 1044 are listed in Table 1 and the EPIC-pn data, the best-fit model and residuals are plotted in Figure 9.

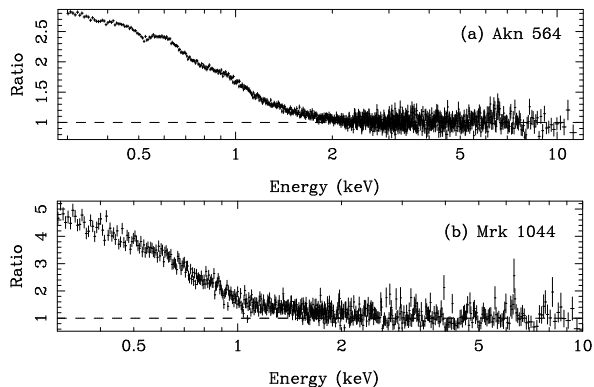


Fig. 7.— Ratios of observed EPIC-pn data for Akn 564 and Mrk 1044 and the corresponding best-fit power-law model fitted above 3 keV and extrapolated to lower energies.

The MCD+PL model was a poor fit for Akn 564 ($\chi^2/dof = 1494.1/913$). Examination of the residuals showed broad emission/absorption features below ~ 1 keV in the spectrum of Akn 564. To verify and investigate these features, we have analyzed the high resolution soft X-ray spectra of Akn 564 obtained with the two RGS simultaneously with the EPIC-pn data. We used the Cash statistic to fit the low count RGS data. We fitted a simple PL model, modified with the neutral absorption, jointly to RGS1 and RGS2 data in the 0.35–1.9 keV band. This resulted in a steep spectrum ($\Gamma \sim 3.0$) and $N_H = 7.6 \times 10^{20} \text{ cm}^{-2}$. Addition of an MCD component improved the fit ($C/dof = 2575.9/1572$; $\Delta C = -225.4$ for two parameters). The best-fit parameters are $N_H \sim 5.2 \times 10^{20} \text{ cm}^{-2}$, $\Gamma \sim 2.44$ and the MCD $kT_{in} \sim 165$ eV. Examination of the ratio of the

data and model revealed a strong absorption feature at ~ 0.5 keV and additional weak and narrow absorption features in the 0.5 – 1 keV band, suggesting the presence of a warm absorber medium in Akn 564.

4.2. Warm absorber model for Akn 564

To describe the weak absorption features seen in the RGS data, we have created a warm absorber model for Akn 564 using the spectral simulation code CLOUDY version 7.02.01 (last described by Ferland et al. 1998). We used a multicomponent ionizing continuum similar to that observed from Akn 564. We used the ‘agn’ continuum available within CLOUDY. This continuum has four parameters: the temperature of the big blue bump emission, the slope of the high energy X-ray continuum, X-ray to UV ratio (α_{ox}) and the UV spectral index. We set the temperature of the big blue bump component and the slope of the high energy continuum to be similar to the temperature of the soft X-ray excess emission and the slope of the hard power law, respectively, derived from the EPIC-pn data. For Akn 564, $\alpha_{ox} = 0.941$ (Gallo 2006) and we used a typical value of -0.5 for the UV spectral index (Elvis et al. 1994; Francis 1993). The X-ray power law is assumed to fall as ν^3 above 100 keV and the big blue component is assumed to have an infra-red exponential cut-off at $kT_{IR} = 0.01$ Ryd or 0.136 eV. We also included the cosmic microwave background radiation so that the incident continuum has nonzero intensity at very long wavelengths. We assumed a plane parallel geometry and calculated grids of models by varying the ionization parameter and the total hydrogen column density. We also included UTA features from Gu et al. (2006) in our calculation. The grid of models were imported to ISIS in the form of an XSPEC-style multiplicative table model as described in Porter et al. (2006).

To describe the weak absorption features in the RGS spectra of Akn 564, we multiplied the CLOUDY warm absorber model to the MCD+PL model. The model was also modified by neutral absorption along the line of sight as before. The addition of the warm absorber component improved the fit ($C/dof = 2469.3/1569$; $\Delta C = -106.6$ for three additional parameters) with warm absorber column, $N_W \sim 4 \times 10^{20} \text{ cm}^{-2}$, ionization parameter ($\log \xi \sim 2$) and the out-

Table 1: Spectral model parameters for Akn 564 and Mrk 1044.

Parameter	Akn 564 ¹	Mrk 1044
MCD+PL		
N_H (10^{20} cm ⁻²)	5.24(f)	3.54(f)
kT_{in} (eV)	179 ± 2	138 ± 3
n_{MCD} ²	3002^{+104}_{-100}	2992^{+316}_{-277}
Γ	2.48 ± 0.01	2.14 ± 0.04
n_{PL} ³	$(1.35 \pm 0.02) \times 10^{-2}$	$(3.2 \pm 0.1) \times 10^{-3}$
$E_{FeK\alpha}$ (keV)	6.72 ± 0.03	6.42 ± 0.04
$f_{FeK\alpha}$ ⁴	$(5.1 \pm 1.8) \times 10^{-6}$	$(1.14 \pm 0.46) \times 10^{-5}$
$f_{0.3-10keV}$ ⁵	6.6×10^{-11}	2.1×10^{-11}
χ^2/dof	919.3/854	611.7/539
Blurred Reflection		
N_H (10^{20} cm ⁻²)	5.24(f)	3.54(f)
Γ	$2.468^{+0.002}_{-0.001}$	$2.20^{+0.002}_{-0.004}$
n_{PL} ³	$9.29 \pm 0.03 \times 10^{-3}$	$1.43^{+0.05}_{-0.03} \times 10^{-3}$
β	≥ 10.0	≥ 10.0
$r_{in}(r_g)$	< 1.58	< 1.25
i	$66 \pm 1^\circ$	$65.7^{+0.3^\circ}_{-0.2^\circ}$
n_{refl} ⁶	$(4.27 \pm 0.02) \times 10^{-7}$	$1.7^{+0.02}_{-0.01} \times 10^{-6}$
A_{Fe}	0.69 ± 0.01	$0.35^{+0.04}_{-0.03}$
ξ (erg cm s ⁻¹)	3452^{+129}_{-114}	$334.5^{+2.1}_{-1.2}$
$E_{FeK\alpha}$ (keV)	$6.72^{+0.05}_{-0.03}$	6.42 ± 0.04
$f_{FeK\alpha}$ ⁴	$2.5^{+2.1}_{-1.5} \times 10^{-6}$	$1.0^{+0.4}_{-0.5} \times 10^{-5}$
$f_{0.3-10keV}$ ⁵	6.4×10^{-11}	2.0×10^{-11}
χ^2/dof	954.2/850	671.6/535
Smeared absorption		
N_H (10^{20} cm ⁻²)	5.24(f)	3.54 (f)
Γ	$2.783^{+0.006}_{-0.008}$	2.49 ± 0.02
n_{PL} ³	$(3.67 \pm 0.05) \times 10^{-2}$	$(7.6 \pm 0.2) \times 10^{-3}$
wind N_H (10^{22} cm ⁻²)	$19.6^{+1.8}_{-0.9}$	$15.7^{+1.8}_{-1.6}$
$\log(\xi/\text{erg cm s}^{-1})$	$2.9^{+0.05}_{-0.03}$	2.89 ± 0.04
σ ⁷	0.81 ± 0.03	0.29 ± 0.03
$E_{FeK\alpha}$ (keV)	6.72 ± 0.03	6.42 ± 0.04
$f_{FeK\alpha}$ ⁴	$(5.1 \pm 2.6) \times 10^{-6}$	$(1.2 \pm 0.5) \times 10^{-5}$
$f_{0.3-10keV}$ ⁵	7.1×10^{-11}	2.1×10^{-11}
χ^2/dof	1147.1/853	592.4/538
Thermal Comptonization		
N_H (10^{20} cm ⁻²)	5.24(f)	3.54 (f)
Γ	2.46 ± 0.01	2.11 ± 0.05
n_{PL} ³	$(1.31 \pm 0.02) \times 10^{-2}$	$(3.1 \pm 0.15) \times 10^{-3}$
kT_{seed} (eV)	30(f)	30(f)
kT_e (keV)	0.176 ± 0.006	$0.137^{+0.012}_{-0.010}$
Γ_{thcomp}	2.1 ± 0.1	2.1 ± 0.2
$E_{FeK\alpha}$ (keV)	6.72 ± 0.03	6.42 ± 0.04
$f_{FeK\alpha}$ ⁴	$(4.9 \pm 1.8) \times 10^{-6}$	$(1.1 \pm 0.5) \times 10^{-5}$
$f_{0.3-10keV}$ ⁵	6.7×10^{-11}	2.1×10^{-11}
χ^2/dof	900.2/853	603.0/538

¹For Akn 564, all models were modified by the two phase warm absorber medium inferred from the RGS data and the EPIC-pn data were fitted in the 0.6 – 11 keV band.

²MCD normalization $n_{MCD} = (R_{in}/km)/(D/10 \text{ kpc})$, where R_{in} is the inner radius and D is the distance.

³Power-law normalization in units of photons keV⁻¹ cm⁻² s⁻¹ at 1 keV.

⁴ine flux in photons keV⁻¹ cm⁻² s⁻¹.

⁵Observed flux in units of ergs cm⁻² s⁻¹ in the 0.3 – 10 keV band.

⁶Normalization of the reflected spectrum.

⁷Gaussian sigma for velocity smearing in units of v/c .

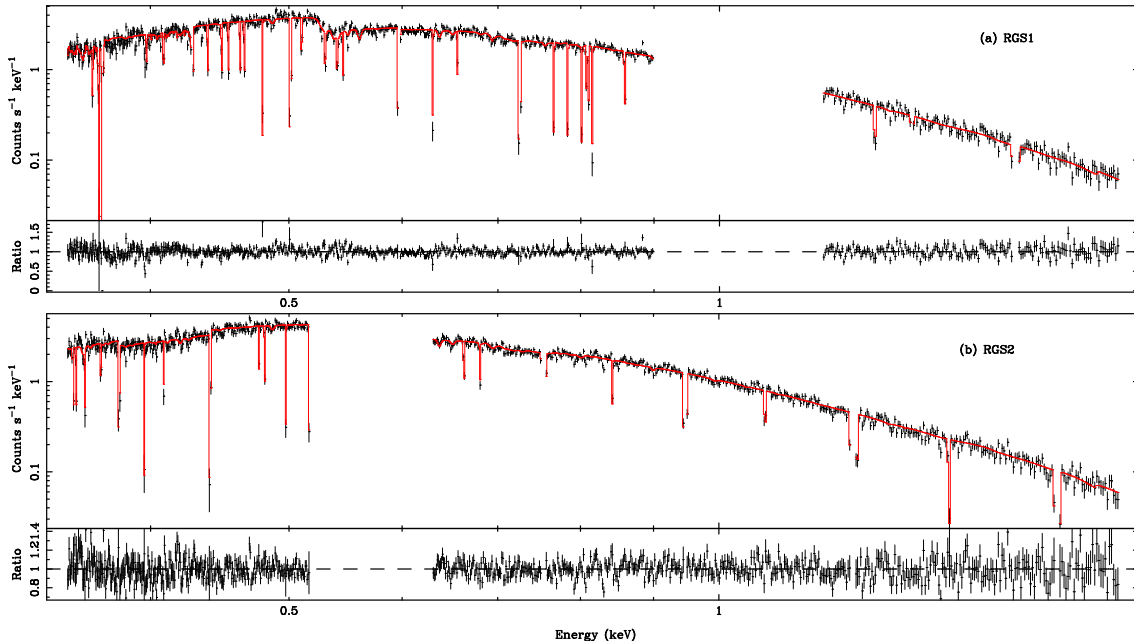


Fig. 8.— (a) RGS1 data, the best-fitting joint model and the ratios of the observed data and the model for Akn 564. (b) The same as (a) but for RGS2. The best-fit model was derived by joint spectral fitting to both RGS1 and RGS2 data.

flow velocity ($v \sim 300 \text{ km s}^{-1}$). An additional warm absorber component further improved the fit ($\Delta C = -70.5$ for three parameters) with $N_W \sim 2 \times 10^{-20} \text{ cm}^{-2}$, $\log \xi < 0.3$ and $v \sim -1000 \text{ km s}^{-1}$. Examination of the residuals showed a strong absorption feature near 0.5 keV at the location of the neutral oxygen edge. However, the shape of the absorption feature does not resemble to an absorption edge, it is similar to an absorption line with a very weak emission line at the center. This feature is likely due to possible RGS calibration errors at the oxygen edge and/or from the Galactic oxygen along the line of sight. Addition of a Gaussian absorption line improved the fit ($\Delta C = -97.3$ for three parameters). The parameters of the best-fit model to the RGS data is listed in Table 2. We note that the best-fit neutral absorption column density derived from the RGS data is $N_H = 5.24^{+0.13}_{-0.03} \times 10^{20} \text{ cm}^{-2}$ which is less than the Galactic column of $6.40 \times 10^{20} \text{ cm}^{-2}$ derived from the HI map of Dickey & Lockman (1990). The best-fit column, however, is consistent with the Galactic column of $5.34 \times 10^{20} \text{ cm}^{-2}$ derived from the Leiden/Argentine/Bonn (LAB) Survey of Galactic HI (Kalbera et al. 2005). McK-

ernan, Yaqoob, & Reynolds (2007) derived cold $N_H = 4^{+2}_{-1} \times 10^{20} \text{ cm}^{-2}$ using the Chandra high energy transmission grating observations of Akn 564. Given the above uncertainties in the measurement of cold N_H , we fix the cold absorption at the best-fit RGS value of $N_H = 5.24 \times 10^{20} \text{ cm}^{-2}$ in all the subsequent fits for Akn 564.

The above analysis clearly shows the presence of a two phase warm absorber medium in Akn 564. Some or all of the emission/absorption features resulting in the poor quality of the fit to the EPIC-pn, described above in section 4.1 are likely due to the presence of warm absorbers. However, it is difficult to determine accurately the parameters of the warm absorber based on the lower resolution EPIC-pn data alone. Therefore, we used the best-fit warm absorber components derived from the RGS data to model the EPIC-pn data. We used the two component warm absorber model with the fixed parameters along with the MCD+PL model and fitted the EPIC-pn data. The addition of the warm absorber components improved the fit, providing $\chi^2/dof = 1654.1/912$. However, the fit is still not acceptable mainly due to a strong absorption feature near 0.5 keV and slight excess of

Table 2: Best-fit model parameters derived from the high resolution RGS observation of Akn 564

Neutral absorption	N_H (10^{20} cm $^{-2}$)	$5.25^{+0.13}_{-0.03}$
Warm absorber I	N_W (10^{20} cm $^{-2}$)	$3.9^{+0.5}_{-0.3}$
	$\log\xi$	2.0 ± 0.1
	$(v/\text{km s}^{-1})$ ^a	-280^{+130}_{-180}
Warm absorber II	N_W (10^{20} cm $^{-2}$)	$2.1^{+0.2}_{-0.1}$
	$\log\xi$	< 0.32
	$(v/\text{km s}^{-1})$ ^a	-1080^{+175}_{-155}
Disk blackbody	kT_{in} (eV)	171 ± 2
	n_{MCD} ^b	2917^{+18}_{-69}
Power law	Γ	2.48 ± 0.01
	n_{PL} ^c	$(1.50 \pm 0.01) \times 10^{-2}$
Absorption line	E (keV)	0.541 ± 0.001
	f_{line} ^d	$-2.6^{+0.5}_{-0.3} \times 10^{-4}$
C/dof		$2301.5/1577$

^aVelocity with respect to the systemic velocity. Negative sign indicates outflow.

^bMCD normalization $n_{MCD} = (R_{in}/km)/(D/10 \text{ kpc})$, where R_{in} is the inner radius and D is the distance.

^cPower-law normalization in units of photons keV $^{-1}$ cm $^{-2}$ s $^{-1}$ at 1 keV.

^dline flux in photons keV $^{-1}$ cm $^{-2}$ s $^{-1}$.

emission below 0.5 keV. The absorption feature is stronger by a factor of ~ 2.5 in the EPIC-pn data than that derived from the RGS data. Also the excess emission below 0.5 keV is not evident in the RGS data. Thus EPIC-pn and RGS do not agree well below 0.6 keV. Therefore we ignore the EPIC-pn data below 0.6 keV in the fits for Akn 564 described below.

After excluding the data below 0.6 keV, the MCD+PL model modified with the two component warm absorber and neutral absorption along the line of sight provided a much better fit ($\chi^2/dof = 941.2/856$). Adding a narrow Gaussian line at ~ 6.6 keV further improved the fit ($\Delta\chi^2/dof = -21.9$ for two parameters). Figure 10 shows the EPIC-pn data, the best-fit model and the χ -residuals and the best-fit parameters are listed in Table 1. The parameters of the MCD and PL components are similar to that derived from the RGS data (see Table 2 and 2). The MCD component used above to describe the soft X-ray excess emission is physically inappropriate. The inner accretion disk temperatures, $kT_{in} = 179 \pm 2$ eV for Akn 564 and 138 ± 3 eV for Mrk 1044 are much

higher than that expected from a disk around a black hole of mass $10^6 - 10^7 M_{\odot}$. For this reason, the origin of the soft excess emission has remained unsolved for more than two decades.

4.3. Relativistically blurred ionized reflection

One possibility is that the reflected emission from a partially ionized accretion disk could be strong below 1 keV and can account for the strong soft excess emission (see e.g., Crummy et al. 2005). Though there is no clear evidence for a broad iron $K\alpha$ line, such a line from an accretion disk could be hidden in the strong X-ray continuum. To test whether the strong soft X-ray excess emission from Akn 564 and Mrk 1044 could be produced by the ionized reflection emission arising from the reprocessing of the primary X-ray emission in the disk, we have fitted the relativistically blurred ionized reflection model to the EPIC-pn spectra of both the NLS1. We used the table model `reflion` (Ross & Fabian 2005; Ross, Fabian & Young 1999) for the ionized reflection and blur the ionized reflection emission relativisti-

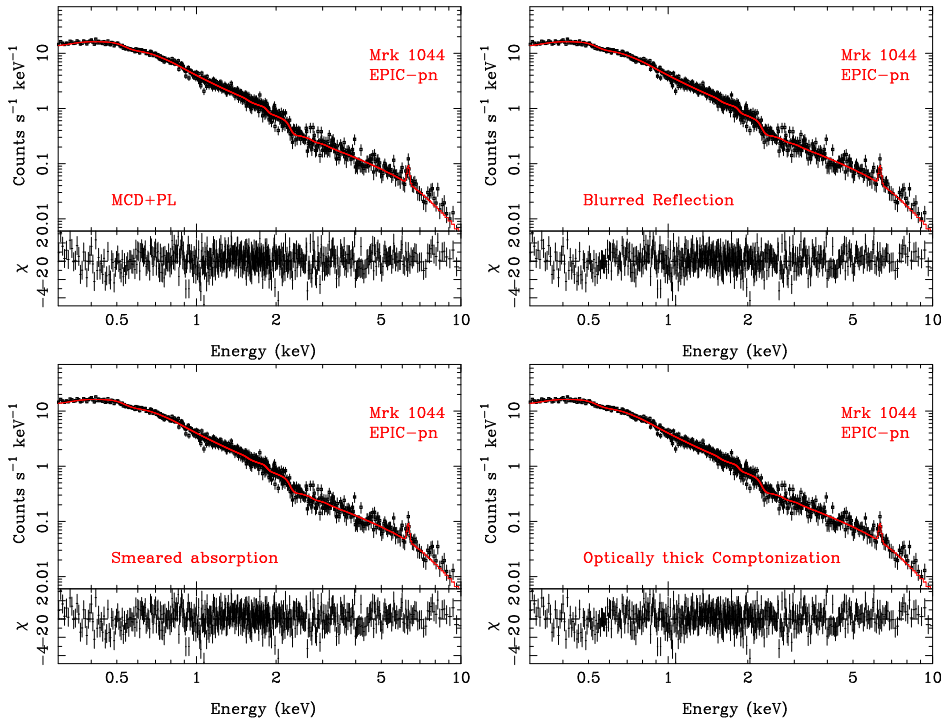


Fig. 9.— Observed EPIC-pn data and the best-fit models for Mrk 1044 corresponding to the best-fit models and their parameters listed in Table 1.

cally by convolving with a LAOR kernel (`kdblur`) to obtain the relativistically broaden ionized reflection from the inner regions of an accretion disk. The parameters of `reflion` model are ionization parameter (ξ), iron abundance relative to solar (A_{Fe}), photon index of the illuminating power-law and the normalization of reflected spectrum. The parameters of the convolution model `kdblur` are the inner and outer radii of the disk (r_{in} and r_{out}), emissivity index (β) and the disk inclination (i). We fixed the outer radius at $r_{out} = 400r_g$ where $r_g = GM/c^2$ is the gravitational radius. We used the power-law component for the continuum. We also used a narrow Gaussian to describe the unresolved iron $K\alpha$ line from distant matter. We also used the two component warm absorber model with the parameters fixed at the values derived from the RGS data. We refer the full model as the blurred reflection model. The best-fit parameters of this model are listed in Table 1. The observed data and the best-fit reflection models are shown in Figure 9 (Mrk 1044) and Figure 10 (Akn 564). The model resulted in poorer fit than the MCD+PL model for both the NLS1

($\chi^2/dof = 954.2/837$ for Akn564 and $671.6/535$ for Mrk 1044). Also the emissivity index is unphysically large ($\beta \geq 10$) and the inner radius is very small for both the AGN, suggesting that the model cannot account for the observed smoothness of the soft excess X-ray emission. The very steep emissivity indices and the small inner radii of the LAOR kernel were required to smooth the recombination features sufficiently to produce the featureless soft X-ray excess emission from both the NLS1s.

4.4. Smeared absorption from partially ionized material

The observed soft excess emission could be an artifact of smeared absorption from partially ionized material as described by Gierlin'ski & Done (2004). To test this scenario, we have fitted the EPIC-pn data with the smeared absorption model. We used the XSPEC local model `swind1` for the smeared absorption from a partially ionized wind from an accretion disk and the simple PL model for the continuum. Again we used a Gaussian

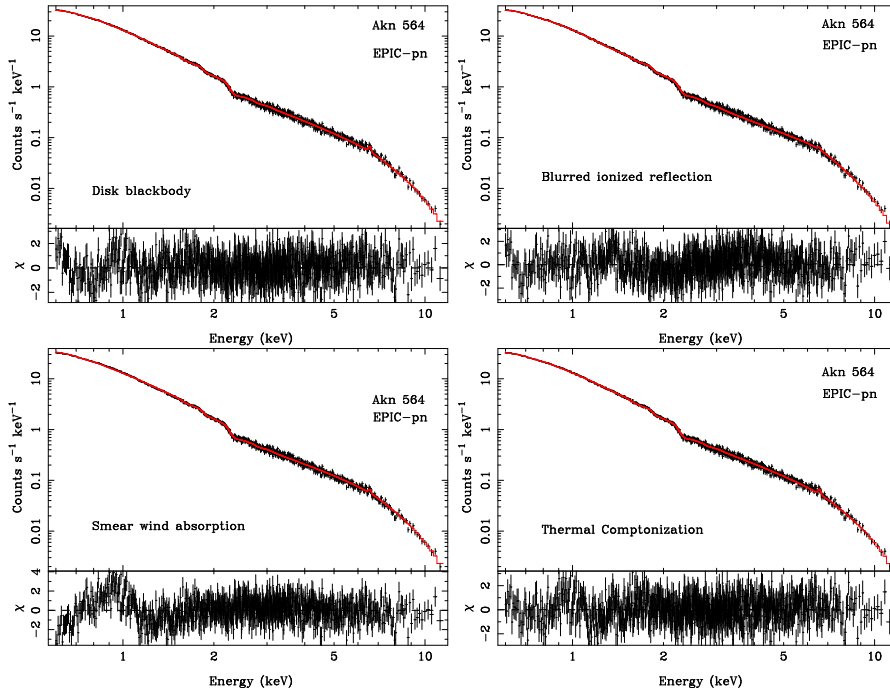


Fig. 10.— Observed EPIC-pn data and the best-fitting MCD+PL, blurred ionized reflection, smeared absorption from partially ionized wind and optically thick thermal Comptonization models for Akn 564. The best-fit parameters are listed in Table 1.

for the narrow iron $K\alpha$ line and the two component warm absorber model with fixed parameters derived from the RGS data. The parameters of the smeared wind model are absorption column density, the ionization parameter ($\xi = L/nr^2$) and the Gaussian sigma for velocity smearing in units of v/c . The smeared absorption model provided a good fit to the spectrum of Mrk 1044 ($\chi^2/dof = 592.4/538$) but fails to describe the spectrum of Akn 564 ($\chi^2/dof = 1147.1/842$). This model requires unphysically large smearing velocity ($\sim 0.8c$) for Akn 564 to smooth sufficiently the absorption lines in order to produce the observed smooth soft excess emission (see Table 1 and Fig. 10).

4.5. Optically-thick, thermal Comptonization

The strong and smooth soft excess emission from NLS1 can also be described as arising from thermal Comptonization in an optically thick corona. To test such a scenario, we used the thermal Comptonization model (ThComp) described

by Zdziarski et al (1996). The free parameters of ThComp model are the asymptotic power-law index (Γ_{thcomp}), electron temperature (kT_e) and the seed photon temperature (kT_{bb}). The electron scattering optical depth (τ) can be calculated from the asymptotic power-law photon index (Γ_{comph}) and electron temperature (kT_e) as follows

$$\alpha = \left[\frac{9}{4} + \frac{1}{(kT_e/m_e c^2)\tau(1 + \tau/3)} \right]^{1/2} - \frac{3}{2} \quad (1)$$

with $\Gamma_{thcomp} = \alpha + 1$ (Sunyaev & Titarchuk 1980). We also used the PL model to describe the hard PL for the hot Comptonized component. We fixed the temperature of the seed photons for the optically thick Comptonization at 30 eV. This is equivalent to assuming that the seed photons for the Comptonizations in the warm and hot plasma arise from the accretion disk. Again we used the narrow Gaussian line for the iron $K\alpha$ line. This model provided good fits for both the NLS1s ($\chi^2/dof = 900.2/842$ for Akn 564 and $\chi^2/dof = 603.0/538$ for Mrk 1044). The best-fit parameters are listed in Table 1 and the EPIC-pn data and

the best-fit model are plotted in Fig. 9 and Fig. 10. The electron temperatures are low (~ 0.18 keV for Akn 564 and ~ 0.14 keV for Mrk 1044) and electron scattering optical depths are very high ($\tau \sim 45$) for both the NLS1s.

We note that the thermal Comptonization model best describes the EPIC-pn data in the 0.6 – 11 keV band for Akn 564 (see Table 1). We expect that the most suitable model must provide a reasonably good fit to the full band EPIC-pn data except for the absorption feature at 0.54 keV, provided that the calibration errors at low energies (< 0.5 keV) are at a level of a few percent. We find that the thermal Comptonization model best describes the full band data with $\chi^2/dof = 1164.8/911$ without any significant change in the best-fit parameters listed in Table 1. Addition of an absorption line at 0.54 keV improved the fit to $\chi^2/dof = 985.5/908$ with line center at $E = 0.54 \pm 0.005$, $f_{line} = -(4.44 \pm 0.06) \times 10^{-4}$ ergs cm $^{-2}$ s $^{-1}$ and width $\sigma < 8$ eV. The ionized reflection and smeared absorption models both fail to describe the data below 0.5 keV when extended to lower energies. Refitting the reflection model with the addition of an absorption line at 0.54 keV to the full band data resulted in poor fit ($\chi^2/dof = 1392.2/906$) with large emissivity index ($\beta = 9.17_{-0.03}^{+0.20}$) and small inner radius ($r_{in} < 1.239r_g$) as before. The smeared absorption model with the addition of the absorption line provided the worst fit among the four models.

5. Discussion

We have studied the X-ray temporal and spectral characteristics of Akn 564 and Mrk 1044. We found that the 0.2 – 2 keV and 2 – 10 keV band lightcurves are strongly correlated without any time delay. However, the strength of this correlation decreases with increasing separation between the soft and hard bands. We have found significant correlation between the soft (0.2 – 0.3 keV, 0.2 – 0.5 keV) and hard (5 – 10 keV, 4 – 10 keV) band lightcurves at positive time delays. The 4 – 10 keV band lags behind the 0.2 – 0.5 keV band by 1767 ± 122 s (at 90%) in Akn 564. We note that Arevalo et al (2006) found time delays that increase both with time scale and energy separation between the energy bands. This means

that there is no single, well defined delay. Instead, the measured delay based on the cross-correlation analysis is the averaged delay between the soft and hard bands. We find no correlation at zero time lag between the 0.2 – 0.3 keV and 5 – 10 keV band emission from Mrk 1044. We confirm the presence of a break at $\sim 1.2 \times 10^{-3}$ Hz in the power density spectrum of Akn 564, earlier detected by Papadakis et al. (2002) based on *ASCA* observations. We also find that the PDS of Akn 564 is energy dependent. The hard band (3 – 10 keV) PDS, consistent with a simple power law, is flatter and stronger than the soft band (0.2 – 0.5 keV) PDS that shows clear evidence for the break. These observations strongly suggest that different variability process dominate the soft and hard band emission. This may suggest physically distinct spectral components for the soft excess and the power-law components.

5.1. Implications of the observed time delays

The observed hard band delays from Akn 564 demonstrate that the soft excess emission cannot be the reprocessed emission of the primary X-ray emission. Fabian et al. (2002) presented the reflection dominated ionized accretion disk model and successfully reproduced the strong soft excess emission from the NLS1 galaxy 1H 0707-495. In this model, the strong soft excess is caused by the multiple reflections of mostly hidden hard X-ray continuum by the clumpy disk and the stronger reflectivity of the partially ionized material below ~ 0.7 keV, associated with an abrupt change in the opacity (Ross, Fabian & Ballantyne 2002; Fabian et al. 2004). The soft X-ray excess emission is the reprocessed emission in this model, hence it is unlikely that the soft X-rays lead the hard X-ray emission. This is, however, not a strong constraint on the ionized reflection model. Many of the soft X-ray lines expected from the accretion disk are excited by soft X-ray photons with energies slightly greater than the line energies as the photoelectric absorption cross section varies as $\sim E^{-3}$. The ionizing soft X-ray photons can lead the hard (3 – 10 keV) band emission due to the Compton delay of hard photons in the Comptonization process. Since the life times of excited states, responsible for the line photons, are very short compared to the expected Compton

delay between the soft and hard photons, the line photons as well as the scattered soft X-ray emission can still lead the hard band primary emission. However, in this case, the soft X-ray excess emission is not expected to show rapid and large amplitude variability as the reflection component and broad iron line are known to show little variability in MCG-6-30-15 (Miniutti et al. 2007). Moreover, the blurred ionized reflection model with physically plausible parameters cannot reproduce the observed soft X-ray excess emission from Akn 564 and Mrk 1044.

Gierlinski & Done (2004) presented an alternative model for the origin of the soft excess emission. In this model, the soft excess emission is mainly due to the strong and smeared absorption near ~ 0.7 keV. The soft excess and the hard power law are part of the same and single continuum component except for the small contribution from smeared emission lines. This means the soft and hard band emission arise from the same continuum component or physical process - Comptonization. The time delay is a natural outcome of the Comptonization process. A general prediction of Comptonization models is that the hard X-ray variations should lag behind those in softer bands (Payne 1980). Therefore it is natural to attribute the observed time delays between hard and soft photons to this process. The time lag represents the difference in the photon escape times between the soft and hard bands. The hard band photons tend to have undergone more scattering events, therefore travel longer and escape the corona later than the soft band photons. Thus the observed time lag is consistent with a single continuum component and hence with the smeared absorption model. However, there are three problems with the smeared wind model. (i) This model (XSPEC local model `swind1`; Gierliński & Done 2004) does not describe the X-ray spectrum of Akn 564 satisfactorily. (ii) The 3 – 10 keV band shows more variability power on short time scales than the 0.2–0.5 keV band, which is not expected in the simple Comptonization models in which the variability is caused by the variations in the seed photons alone. (iii) The smearing velocity for Akn 564 suggested by the `swind1` model is very large ($v \sim 0.8c$) for disk winds. Hydrodynamical simulations show that the line driven winds do not have the required smearing velocity (N. J. Schurch,

private communication). It remains to be seen if the magnetically driven winds can provide the required smearing.

The two component model, Comptonization in two separate regions, is a viable option. In this model, the soft excess emission arises from the Comptonization in the low temperature (warm), optically thick plasma while the hard power-law is produced by the Comptonization in the hot plasma. Indeed the EPIC-pn spectra of Akn 564 and Mrk 1044 are both well described by the two component model. The temperature of the warm plasma is ~ 175 eV for Akn 564 and ~ 135 eV for Mrk 1044. This region, giving rise the soft excess emission, is optically thick ($\tau \sim 45$). Physically, this component could be the warm skin on the accretion disk surface or a region between the disk and an optically thin inner flow (Magdziarz et al. 1998) or an optically thick corona coupled with a truncated disk (Done & Kubota 2006). Depending on the geometry of the disk and the two component corona system, there can be delay between the soft excess and high energy power-law components.

However, the two component Comptonization model has difficulty in explaining the constancy of the temperature of the Comptonizing region producing the soft excess emission. Gierlinski & Done (2004) derived the temperature of the putative Comptonizing region in the range 0.1 – 0.2 keV which is remarkably constant for 26 different PG quasars. They concluded that the constancy of the temperature is inconsistent with that expected from the span of the asymptotic power-law index ($\Gamma_{thcomp} \sim 1.5 - 2.5$). However, the 0.3 – 10 keV *XMM-Newton* band only includes the high energy tail of the optically thick Comptonized emission. Both the peak of the soft excess component ($kT \sim 0.1 - 0.2$ keV) and the asymptotic power-law component fall below 0.3 keV. Using such data, it may be difficult to measure accurately both the temperature and the asymptotic photon index, particularly in the presence of line of sight neutral absorption and complex warm absorber, both modifying the soft X-ray spectrum below 1 keV. NLS1 galaxies show a large diversity in their soft X-ray *ROSAT* photon indices ($\Gamma \sim 1.5 - 5.0$), suggesting varying shape of the soft excess component (Boller, Brandt & Fink 1996). The constancy of the temperature for the

soft excess emission is required to be investigated using a sample of NLS1 galaxies similar to that used by Boller, Brandt & Fink (1996). Another possibility is that the disk/corona geometry is different in NLS1 galaxies as they are accreting close to the Eddington rate. In such situations, the inner disk is likely thick and hotter. It remains to be seen if such thick structure can have uniform temperatures across AGN with a large range in their luminosity and black hole masses.

5.2. The disk-corona geometry

Inverse Compton scattering by thermal electrons provides the best possible explanation for the observed smooth soft X-ray excess emission from Akn 564 and Mrk 1044. Our spectral analysis favors two physically distinct corona: high optical depth, low temperature corona and high temperature, low optical depth corona. There are two possible geometries with two component corona. The cool, optically thick corona may be similar to the coupled disk corona geometry proposed by Done & Kubota (2006) for the very high state of black hole binaries. In this geometry, the inner accretion disk is truncated and is coupled to an optically thick corona, and gravitational energy release powers both the disk and the optically-thick corona. Comptonization of the disk photons in this corona may give rise to the broad soft excess component. In addition to the optically thick corona, a hot corona is responsible for the power-law component. The hot corona could be the same as the patchy corona above the disk and is likely powered by magnetic flares in the disk similar to the solar flares (Haardt, Maraschi, & Ghisellini 1994; Stern et al. 1995; Poutanen & Svensson 1996; Poutanen & Fabian 1999; Merloni & Fabian 2001). The seed photons could either be the soft photons from the disk or those arising from the cool, optically thick corona. Since the disk is coupled to the optically thick corona, appreciable time lag between the disk photons and the soft excess photons are not expected. The variability of the disk flux and the soft excess emission is governed by the variations in the accretion rate, while the variability of the power-law component is governed both by the variation in the soft photons as well as any variability process intrinsic to the corona such as that related to variation in the electron population. The flatter power density spectrum

of Akn 564 in the hard band may be related to the additional variability of the power-law component due to the changes in electron population on short time scales e.g., caused by magnetic flares above the accretion disk.

Another possible geometry is the ionized surface of a disk acting as an optically thick and cool corona with a temperature of $\sim 0.1 - 0.3$ keV (e.g, Magdziarz et al. 1998; see also O’Brian et al. 2001; Page et al. 2002; Vaughan et al. 2002). In this case, thermal Comptonization of disk photons by thermal electrons in the hot surface of the disk will produce the smooth soft excess. The steep power-law extending to high energies can be produced in another purely hot thermal/nonthermal or in a hybrid thermal-nonthermal plasma.

It is difficult to distinguish the two geometries described above. The different power spectra of the soft and hard band X-ray emission may constrain the two geometries. Recently McHardy et al. (2006) have shown a strong correlation between the break frequency, black hole mass and the bolometric luminosity for black hole binaries and AGN. If the break frequencies are related to the characteristic radii from the central source, their result suggests a characteristic size that appears to decrease with increasing accretion rate or luminosity. The clear evidence for a break in the soft band PDS of Akn 564 suggests a characteristic size associated with the soft X-ray excess emission which can be the size of the optically thick corona or the radius of the inner truncated disk in the model suggested by Done & Kubota (2006). It is also possible that the disk surface below an inner radius is ionized and the temperature of the inner disk surface is higher than that expected from the standard disk. The inner disk surface may then be responsible for the soft excess emission. The lack of a clear break in the hard band PDS of Akn 564 may suggest that power-law emission is probably not associated with a characteristic size and it arises from an extended corona similar to a patchy corona above an accretion disk. Future long observations of Akn 564 are required to clearly demonstrate the presence or absence of a break in the hard band PDS.

6. Conclusions

We have presented temporal and spectral study of *XMM-Newton* observations of Akn 564 and Mrk 1044. The main results are as follows:

1. The 0.2 – 2 keV and 2 – 10 keV band X-ray emission from both the NLS1 galaxies are strongly correlated without any time delay. However, the variations in the 0.2 – 0.5 keV band are found to lead those in the 4 – 10 keV band by 1768 ± 122 s (90%) in Akn 564. We do not find any correlation between the 0.2–0.3 keV and 5–10 keV X-ray emission from Mrk 1044 at zero time delay. The two bands appear to anti-correlate at a positive lag of ~ 1000 s and likely correlated at a lag of $\sim 3000 - 5000$ s. Long observations of Mrk 1044 are required to confirm the time delay.
2. The full band power density spectrum of Akn 564 has a break at $(1.2 \pm 0.3) \times 10^{-3}$ Hz, corresponding to a time scale of ~ 1000 s, similar to the delay between 0.2 – 0.5 and 4 – 10 keV bands. It is not clear if there is any physical relation between the two time scales. There is a clear evidence of a break in the soft band PDS but the hard band does not show a clear evidence for the break.
3. The soft (0.2 – 0.5 keV) band PDS of Akn 564 is significantly steeper and weaker than the hard (3 – 10 keV) band PDS. This implies that the power-law component is more variable than the soft excess component on shorter time scales. The implication of this result on the Comptonization models is that the variations in the power-law component are not only caused by the variations in the seed photons but also by the variations in the hot electron population. Thus electron injection on short time scales ($\lesssim 1000$ s) are required. This could be evidence for magnetic flares thought to power the corona above the accretion disk.
4. The soft excess emission from Mrk 1044 is featureless in the EPIC-pn data and is well described by the smeared absorption or optically thick Comptonization. The RGS data show evidence for warm absorbers in

Akn 564. The EPIC-pn spectrum of Akn 564 is well described by a complex model consisting of optically thick thermal Comptonization in a low temperature (~ 0.15 keV) plasma and a steep power-law, modified by two phase warm absorber medium and the Galactic absorption. The ionized reflection and smeared wind models fail to describe the data satisfactorily.

5. The temporal and spectral characteristics of Akn 564 and Mrk 1044 are consistent with a two component corona – a compact low temperature, optically thick corona and an extended hot corona. The compact corona could be an inner optically thick region coupled to a truncated disk or the ionized surface of an inner untruncated disk. The soft excess emission can be produced in the inner, optically thick corona and the power-law component is produced in the hot corona.

We are grateful to the referee, I. Papadakis, for his detailed comments and suggestions that improved this paper significantly. We thank M. Nowak for writing a number of useful ISIS functions that have been used in this paper. GCD gratefully acknowledges the support of NASA grants NNX07AE99G and NNX06AE38G. This work is based on observations obtained with *XMM-Newton*, an ESA science mission with instruments and contributions directly funded by ESA Member States and the USA (NASA). This research has made use of data obtained through the High Energy Astrophysics Science Archive Research Center Online Service, provided by the NASA/Goddard Space Flight Center.

REFERENCES

- Arévalo, P., Papadakis, I. E., Uttley, P., McHardy, I. M., & Brinkmann, W. 2006, *MNRAS*, 372, 401
- Arnaud, K. A., et al. 1985, *MNRAS*, 217, 105
- Boller, T., Brandt, W. N., & Fink, H. 1996, *A&A*, 305, 53
- Brinkmann, W., Papadakis, I. E., & Raeth, C. 2007, *A&A*, 465, 107

- Collinge, M. J. et al. 2001, *ApJ*, 557, 2
- Crummy, J., Fabian, A. C., Gallo, L., & Ross, R. R. 2006, *MNRAS*, 365, 1067
- Czerny, B., Niłojajuk, M., Rózańska, A., Dumont, A.-M., Loska, Z., & Zycki, P. T. 2003, *A&A*, 412, 317
- Dasgupta, S., & Rao, A. R. 2006, *ApJ*, 651, L13
- Dewangan, G. C., Boller, T., Singh, K. P., & Leighly, K. M. 2002, *A&A*, 390, 65
- Dickey, J. M., & Lockman, F. J. 1990, *ARA&A*, 28, 215
- Done, C., & Kubota, A. 2006, *MNRAS*, 843
- Elvis, M., et al. 1994, *ApJS*, 95, 1
- Fabian, A. C., Ballantyne, D. R., Merloni, A., Vaughan, S., Iwasawa, K., & Boller, T. 2002, *MNRAS*, 331, L35
- Fabian, A. C., Miniutti, G., Gallo, L., Boller, T., Tanaka, Y., Vaughan, S., & Ross, R. R. 2004, *MNRAS*, 353, 1071
- Fabian, A. C., Miniutti, G., Iwasawa, K., & Ross, R. R. 2005, *MNRAS*, 361, 795
- Ferland, G. J., Korista, K. T., Verner, D. A., Ferguson, J. W., Kingdon, J. B., & Verner, E. M. 1998, *PASP*, 110, 761
- Francis, P. J. 1993, *ApJ*, 407, 519
- Gallo, L. C., Boller, T., Tanaka, Y., Fabian, A. C., Brandt, W. N., Welsh, W. F., Anabuki, N., & Haba, Y. 2004, *MNRAS*, 347, 269
- Gallo, L. C. 2006, *MNRAS*, 368, 479
- Gierliński, M., & Done, C. 2004, *MNRAS*, 349, L7
- Gierliński, M., & Done, C. 2006, *MNRAS*, 371, L16
- Goad, M. R., Roberts, T. P., Reeves, J. N., & Uttley, P. 2006, *MNRAS*, 365, 191
- Gondoin, P., Orr, A., Lumb, D., & Santos-Lleo, M. 2002, *A&A*, 388, 74
- Gu, M. F., Holczer, T., Behar, E., & Kahn, S. M. 2006, *ApJ*, 641, 1227
- Haardt, F., Maraschi, L., & Ghisellini, G. 1994, *ApJ*, 432, L95
- Houck, J. C., & Denicola, L. A. 2000, *Astronomical Data Analysis Software and Systems IX*, 216, 591
- Houck, J. C. 2002, *High Resolution X-ray Spectroscopy with XMM-Newton and Chandra*, Proceedings of the international workshop held at the Mullard Space Science Laboratory of University College London, Holmbury St Mary, Dorking, Surrey, UK, October 24 - 25, 2002, Ed. Branduardi-Raymont, G., published electronically.
- Kalberla, P. M. W., Burton, W. B., Hartmann, D., Arnal, E. M., Bajaja, E., Morras, R., Pöppel, W. G. L. 2005, *A&A*, 440, 775
- Mason, K. O., et al. 2003, *ApJ*, 582, 95
- McHardy, I. M., Koering, E., Knigge, C., Uttley, P., & Fender, R. P. 2006, *Nature*, 444, 730
- McKernan, B., Yaqoob, T., & Reynolds, C. S. 2007, *MNRAS*, 379, 1359
- Magdziarz, P., Blaes, O. M., Zdziarski, A. A., Johnson, W. N., & Smith, D. A. 1998, *MNRAS*, 301, 179
- Markoff, S., Nowak, M. A., & Wilms, J. 2005, *ApJ*, 635, 1203
- Merloni, A., & Fabian, A. C. 2001, *MNRAS*, 328, 958
- Papadakis, I. E., & Lawrence, A. 1993, *MNRAS*, 261, 612
- Papadakis, I. E., Brinkmann, W., Negoro, H., & Gliozzi, M. 2002, *A&A*, 382, L1
- Papadakis, I. E., Brinkmann, W., Page, M. J., McHardy, I., & Uttley, P. 2007, *A&A*, 461, 931
- Payne, D. G. 1980, *ApJ*, 237, 951
- Peterson, B. M., Wanders, I., Horne, K., Collier, S., Alexander, T., Kaspi, S., & Maoz, D. 1998, *PASP*, 110, 660
- Porter, R. L., Ferland, G. J., Kraemer, S. B., Armentrout, B. K., Arnaud, K. A., & Turner, T. J. 2006, *PASP*, 118, 920

- Pounds, K. A., Done, C., & Osborne, J. P. 1995, MNRAS, 277, L5
- Pravdo, S. H., Nugent, J. J., Nousek, J. A., Jensen, K., Wilson, A. S., & Becker, R. H. 1981, ApJ, 251, 501
- Poutanen, J., & Svensson, R. 1996, ApJ, 470, 249
- Poutanen, J., & Fabian, A. C. 1999, MNRAS, 306, L31
- Romano, P., Turner, T. J., Mathur, S., & George, I. M. 2002, ApJ, 564, 162
- Ross, R. R., Fabian, A. C., & Ballantyne, D. R. 2002, MNRAS, 336, 315
- Schurch, N. J., & Done, C. 2006, MNRAS, 762
- Singh, K. P., Garmire, G. P., & Nousek, J. 1985, ApJ, 297, 633
- Sobolewska, M., & Done, C. 2005, AIP Conf. Proc. 774: X-ray Diagnostics of Astrophysical Plasmas: Theory, Experiment, and Observation, 774, 317
- Stern, B. E., Poutanen, J., Svensson, R., Sikora, M., & Begelman, M. C. 1995, ApJ, 449, L13
- Stobbart, A.-M., Roberts, T. P., & Wilms, J. 2006, MNRAS, 368, 397
- Sunyaev, R. A., & Titarchuk, L. G. 1980, A&A, 86, 121
- Strüder, L. et al. 2001, A&A, 365, L18
- Turner, M. J. L. et al. 2001a, A&A, 365, L27
- Turner, T. J., et al. 2001b, ApJ, 548, L13
- Turner, T. J., Romano, P., George, I. M., Edelson, R., Collier, S. J., Mathur, S., & Peterson, B. M. 2001, ApJ, 561, 131
- Zdziarski, A. A., Johnson, W. N., & Magdziarz, P. 1996, MNRAS, 283, 193
- Zdziarski, A. A., & Gierliński, M. 2004, Progress of Theoretical Physics Supplement, 155, 99